Biomedical Optics EXPRESS

Nanoscale refractive index fluctuations detected via sparse spectral microscopy

John E. Chandler, Lusik Cherkezyan, Hariharan Subramanian, and Vadim Backman*

Department of Biomedical Engineering, Northwestern University, 2145 Sheridan Road, Evanston, Illinois, 60208, USA

**v-backman@northwestern.edu*

Abstract: Partial Wave Spectroscopic (PWS) Microscopy has proven effective at detecting nanoscale hallmarks of carcinogenesis in histologically normal-appearing cells. The current method of data analysis requires acquisition of a three-dimensional data cube, consisting of multiple images taken at different illumination wavelengths, limiting the technique to data acquisition on ~30 individual cells per slide. To enable high throughput data acquisition and whole-slide imaging, new analysis procedures were developed that require fewer wavelengths in the same 500-700nm range for spectral analysis. The nanoscale sensitivity of the new analysis techniques was validated (i) theoretically, using finite-difference time-domain solutions of Maxwell's equations, as well as (ii) experimentally, by measuring nanostructural alterations associated with carcinogenesis in biological cells.

OCIS codes: (110.4234) Multispectral and hyperspectral imaging; (170.6510) Spectroscopy, tissue diagnostics; (170.0170) Medical optics and biotechnology; (170.4580) Optical diagnostics for medicine; (170.0110) Imaging systems; (170.1610) Clinical applications

References and links

1. R. Siegel, J. Ma, Z. Zou, and A. Jemal, "Cancer Statistics, 2014," CA Cancer J. Clin. **64**(1), 9–29 (2014).
2. J. R. Gilbertson, J. Ho, L. Anthony, D. M. Jukic, Y. Yagi, and A. V. Parwani, "Primary histologic diagnosis using automated whole slide imaging: a validation study," BMC Clin. Pathol. **6**(1), 4 (2006).
3. T. M. Elsheikh, R. M. Austin, D. F. Chhieng, F. S. Miller, A. T. Moriarty, and A. A. Renshaw; American Society of Cytopathology, "American Society of Cytopathology workload recommendations for automated Pap test screening: Developed by the productivity and quality assurance in the era of automated screening task force," Diagn. Cytopathol. **41**(2), 174–178 (2013).
4. W. S. Campbell, S. M. Lele, W. W. West, A. J. Lazenby, L. M. Smith, and S. H. Hinrichs, "Concordance between whole-slide imaging and light microscopy for routine surgical pathology," Hum. Pathol. **43**(10), 1739–1744 (2012).
5. S. Al-Janabi, A. Huisman, A. Vink, R. J. Leguit, G. J. Offerhaus, F. J. ten Kate, and P. J. van Diest, "Whole slide images for primary diagnostics of gastrointestinal tract pathology: a feasibility study," Hum. Pathol. **43**(5), 702–707 (2012).
6. H. Subramanian, P. Pradhan, Y. Liu, I. R. Capoglu, X. Li, J. D. Rogers, A. Heifetz, D. Kunte, H. K. Roy, A. Taflove, and V. Backman, "Optical methodology for detecting histologically unapparent nanoscale consequences of genetic alterations in biological cells," Proc. Natl. Acad. Sci. U.S.A. **105**(51), 20118–20123 (2008).
7. L. Cherkezyan, I. Capoglu, H. Subramanian, J. D. Rogers, D. Damania, A. Taflove, and V. Backman, "Interferometric spectroscopy of scattered light can quantify the statistics of subdiffractional refractive-index fluctuations," Phys. Rev. Lett. **111**(3), 033903 (2013).
8. D. P. Slaughter, H. W. Southwick, and W. Smejkal, "Field cancerization in oral stratified squamous epithelium; clinical implications of multicentric origin," Cancer **6**(5), 963–968 (1953).
9. L. Cherkezyan, Y. Stypula-Cyrus, H. Subramanian, C. White, M. Dela Cruz, R. K. Wali, M. J. Goldberg, L. K. Bianchi, H. K. Roy, and V. Backman, "Nanoscale changes in chromatin organization represent the initial steps of tumorigenesis: a transmission electron microscopy study," BMC Cancer **14**(1), 189 (2014).
10. H. Subramanian, H. K. Roy, P. Pradhan, M. J. Goldberg, J. Muldoon, R. E. Brand, C. Sturgis, T. Hensing, D. Ray, A. Bogojevic, J. Mohammed, J. S. Chang, and V. Backman, "Nanoscale cellular changes in field carcinogenesis detected by partial wave spectroscopy," Cancer Res. **69**(13), 5357–5363 (2009).

#252091 Received 19 Oct 2015; revised 9 Jan 2016; accepted 2 Feb 2016; published 19 Feb 2016

11. H. K. Roy, C. B. Brendler, H. Subramanian, D. Zhang, C. Maneval, J. Chandler, L. Bowen, K. L. Kaul, B. T. Helfand, C. H. Wang, M. Quinn, J. Petkewicz, M. Paterakos, and V. Backman, "Nanocytological field carcinogenesis detection to mitigate overdiagnosis of prostate cancer: a proof of concept study," PLoS One **10**(2), e0115999 (2015).
12. V. J. A. Konda, L. Cherkezyan, H. Subramanian, K. Wroblewski, D. Damania, V. Becker, M. H. R. Gonzalez, A. Koons, M. Goldberg, M. K. Ferguson, I. Waxman, H. K. Roy, and V. Backman, "Nanoscale markers of esophageal field carcinogenesis: potential implications for esophageal cancer screening," Endoscopy **45**(12), 983–988 (2013).
13. J. E. Chandler, H. Subramanian, C. D. Maneval, C. A. White, and V. Backman, "High-speed spectral nanocytlogy for early cancer detection," J. Biomed. Opt. **18**(11), 117002 (2013).
14. L. Cherkezyan, H. Subramanian, and V. Backman, "What structural length scales can be detected by the spectral variance of a microscope image?" Opt. Lett. **39**(15), 4290–4293 (2014).
15. L. Cherkezyan, H. Subramanian, V. Stoyneva, J. D. Rogers, S. Yang, D. Damania, A. Taflove, and V. Backman, "Targeted alteration of real and imaginary refractive index of biological cells by histological staining," Opt. Lett. **37**(10), 1601–1603 (2012).
16. A. Taflove and S. C. Hagness, *Computational Electrodynamics* (Artech house, 2005).
17. İ. R. Capoglu, J. D. Rogers, A. Taflove, and V. Backman, "The microscope in a computer: Image synthesis from three-dimensional full-vector solutions of Maxwell's equations at the nanometer scale," Prog. Opt. **57**, 1–91 (2012).
18. I. R. Capoglu, A. Taflove, and V. Backman, "Angora: A free software package for finite-difference time-domain electromagnetic simulation," IEEE Antennas and Propagation Mag. **55**(4), 80–93 (2013).
19. D. J. Cook, "Cellular pathology: Introduction to Techniques and Applications," (Scion, Bloxham, 2006).
20. G. C. Crossmon, "Mounting media for phase microscope specimens," Stain Technol. **24**(4), 241–247 (1949).
21. J. M. Schmitt and G. Kumar, "Optical scattering properties of soft tissue: a discrete particle model," Appl. Opt. **37**(13), 2788–2797 (1998).
22. N. Ikeda, C. MacAulay, S. Lam, J. LeRiche, P. Payne, D. Garner, C. Konaka, H. Kato, and B. Palcic, "Malignancy associated changes in bronchial epithelial cells and clinical application as a biomarker," Lung Cancer **19**(3), 161–166 (1998).
23. M. Us-Krasovec, J. Erzen, M. Zganec, M. Strojan-Flezar, J. Lavrencak, D. Garner, A. Doudkine, and B. Palcic, "Malignancy associated changes in epithelial cells of buccal mucosa: a potential cancer detection test," Analytical and quantitative cytology and histology / the International Academy of Cytology. American Society of Cytology **27**, 254–262 (2005).

1. Introduction

Reducing cancer mortality rates is a significant health concern and early detection has been recognized as a key factor in this effort [1]. Screening tools such as whole-slide microscopy and digital pathology have enabled greater throughput and improved rates of lesion detection, particularly when used in conjunction with the Pap (Papanicolaou) test for cervical cancer screening [2, 3]. Multiple studies have also shown concordance between whole slide imaging/digital pathology instruments and light microscopy in diagnostic applications [2, 4] [5]. Despite these results, whole-slide imaging has been limited in its application as a minimally invasive screening technique due to a lack of easily accessible organ sites that harbor biomarkers of disease detectable with the diffraction-limited resolution of current whole-slide imaging systems.

Partial Wave Spectroscopic (PWS) microscopy is a spectroscopic microscopy technique that has proven to be sensitive to changes associated with early carcinogenesis. PWS microscopy achieves sensitivity to nanoscale structures within biological cells by using the spectroscopic content of microscope images, and quantitatively measures nanoarchitectural changes in cells associated with carcinogenesis [6, 7]. These intracellular, macromolecular alterations are recognizable as some of the earliest indicators of carcinogenesis and are detectable throughout an affected organ, not just at the tumor site, via a phenomenon known as the field effect of carcinogenesis [8, 9]. Because PWS is sensitive to nanoscale structure below the diffraction limit of traditional microscopy systems, including those used for whole-slide imaging, it can be used for minimally invasive cancer screening via the field effect. In previous clinical experiments, PWS has been shown to be effective at detecting tumors in multiple organ sites, including the lung, colon, esophagus, pancreas, prostate, etc [10–12].

While PWS microscopy has demonstrated nanoscale sensitivity and diagnostic capability with several major forms of cancer, its throughput has been poor due to the requirement of

#252091 Received 19 Oct 2015; revised 9 Jan 2016; accepted 2 Feb 2016; published 19 Feb 2016

collecting ~200 wavelengths from the visible spectrum (500-700nm with 1nm sampling) for quantitative data analysis. As a result, performance of the technique has been limited, even with the current high-throughput version of the instrument, which utilizes an acousto-optic tunable filter (AOTF) for high speed spectral filtering [13]. To improve the performance of PWS microscopy and extend its capabilities to measurements of larger samples such as tissue sections, a whole-slide imaging approach has been developed. Specifically, changes in the analysis and acquisition procedures have been introduced to reduce the number of wavelengths collected, allowing an order of magnitude improvement in the time for data collection and analysis.

2. Experimental methods

2.1 Instrumentation and data acquisition

To collect high-resolution spectral data cubes (x,y,λ), a recently developed High-Throughput version of the PWS microscope was used [13]. This instrument used an AOTF (HSI-300, Gooch and Housego, Orlando, Florida) for spectral filtration of the Epi-illumination light from a Xenon lamp (66907-100XF-R1, Newport Corporation, Irvine, California) in combination with a high-speed collection camera (Hamamatsu ORCA Flash 2.8, Bridgewater, New Jersey). Unique spectra were obtained from each spatial position within a sample using a low illumination numerical aperture (NA ~0.15) to approximate plane wave illumination and a high collection NA (NA ~0.6) was used with a total magnification of approximately 40X (LUCPlanFL N, Olympus, Center Valley, Pennsylvania). The total magnification of the system ensured that the pixel size at the sample plane was less than the diffraction limited resolution. An automated sample stage (LSQ075B-E01, Zaber Technologies, Vancouver, BC) allowed rapid and programmable collection from multiple fields of view as well as whole-slide imaging. For full-spectrum data collection, 500-700nm with 1nm sampling, a subset of the cell population on a sample slide was measured, typically ~30 cells. These cells were selected manually by a user from a low resolution whole-slide image before high-resolution spectral imaging was performed. Whole-slide spectral imaging was achieved by reducing the number of wavelengths measured from 201 in the full-spectrum approach to 15 wavelengths over the same range from 500 to 700nm. With this approach spectral measurements of the entire cell population on a sample slide were completed in a single acquisition step.

2.2 Full-spectrum analysis

Nanoscale sensitivity of the PWS microscope has been achieved via a spectral analysis technique that utilizes light in the visible spectrum, 500-700nm with 1nm sampling. While the PWS instrument has diffraction limited spatial imaging resolution as expected for a far field optical microscope, the spectrum of the scattered light at each pixel in the image from weakly scattering samples contains information sufficient to quantify 3-D refractive index fluctuations at length scales well below the diffraction limit [7]. When cells mounted on a glass slide and exposed to air are spectrally imaged in the Epi-illumination configuration of the PWS microscope the standard deviation of the spectrum of the scattered light at each pixel (Σ) quantifies the refractive index fluctuations at nanometer length scales limited only by the signal-to-noise ratio of the system [7]. For a sample with exponentially-correlated spatial RI distribution with standard deviation σ_n and characteristic length scale l_c, Σ is defined by Eq. (1), where NA is the numerical aperture of light collection, k_c is the central wavenumber of the bandwidth of light, and Γ is composed of Fresnel coefficients to account for light reflection and transmission at the sample-air interface [7].

#252091 Received 19 Oct 2015; revised 9 Jan 2016; accepted 2 Feb 2016; published 19 Feb 2016

$$\Sigma^2 = \Gamma^2 {\sigma_n}^2 \left[\frac{2k_c L}{\pi} \frac{k_c{}^3 l_c^3 NA^2}{\left(1+4k_c{}^2 l_c^2\right)\left(1+k_c{}^2 l_c^2 (4+NA^2)\right)} + \left(1-1/\sqrt{1+k_c{}^2 l_c^2 NA^2}\right)/4 \right] \quad (1)$$

Using this approach it has been shown that given a 5% noise floor, PWS microscopy is sensitive to a range of length scales from ~22nm to at least 200nm depending on sample structure and thickness [14]. Thus, PWS is a promising tool for detecting early-stage microscopically undetectable tumorigenic alterations in biological cells and tissues such as changes in chromatin organization [9].

2.3 New sparse-spectrum analysis algorithms

The full-spectrum analysis employed originally was designed to maximize the SNR by oversampling both in spatial (multiple image pixels per diffraction-limited spot) and spectral (multiple wavelengths sampled within the spectral resolution of the detector) dimensions ensuring that a spatially-resolved image Σ(x,y) could be generated. As a result of this oversampling, data acquisition and analysis can be modified when the SNR is high to prioritize speed. New analysis algorithms specifically for sparse spectral data have been developed for PWS microscopy to increase the speed of data collection and processing allowing for whole-slide imaging with the PWS microscope. These new methods allow the number of wavelengths used for analysis and thus the number of wavelengths collected to be reduced from a 1nm sampling step size covering the visible spectrum (500-700 nm) to a sparse spectrum consisting of 15 wavelengths covering the same spectral range.

These 15 wavelengths are unevenly spaced with the highest concentration between 540 and 560nm and the remainder distributed evenly over the entire 500-700nm range. This distribution balances spectral resolution and range over the spectrum of interest and allows quantification of the refractive index fluctuations from the signal, maintaining nanoscale sensitivity. Specifically, the new sparse spectrum includes the wavelengths: 500, 525, 540, 543, 546, 549, 552, 555, 558, 575, 600, 625, 650, 675, and 700nm. The densely spaced wavelengths improve diagnostic performance in stained samples when centered at the most diagnostic wavelengths due to an amplification of scattering that corresponds to the absorption spectrum of the dye [15]. In unstained samples, this region can be chosen arbitrarily since similar diagnostic performance can be achieved with any wavelengths. Since we used Papanicolaou stain on some samples in this study, we chose to center the more densely sampled wavelength region around the most diagnostic wavelength for this staining protocol, 550nm. Using these wavelengths two new markers for spectral analysis have been developed and have been shown to be equivalent to the Σ parameter currently used for full-spectrum analysis.

2.4 Spatial analysis at a single wavelength, ($\Sigma_{x,y}$)

The first such marker is the spatial standard deviation of reflectance ($\Sigma_{x,y}$). When imaging capabilities are not required, it is possible to take advantage of the mathematical fact that the standard deviation of reflectance evaluated at one wavenumber, ($\Sigma_{x,y}$) is equivalent to the standard deviation of reflectance across wavelengths averaged over a region of pixels. As a result, the only difference between Σ given in Eq. (1) and $\Sigma_{x,y}$ is the wavenumber k. Σ is evaluated at the central wavenumber, k_c, while $\Sigma_{x,y}$ is evaluated at the chosen single wavenumber k. To increase SNR, we evaluated $\Sigma_{x,y}$ at several wavelengths (centered at k_c), and averaged the obtained values. Experimentally, $\Sigma_{x,y}$ is calculated using Eq. (2), where $R(x,y)$ is the reflectance intensity at the pixel (x,y), and $N_{x,y}$ is the total number of pixels in the region of interest. In addition, since $\Sigma_{x,y}$ can be calculated at any individual wavelength, it can be used to determine the most diagnostic wavelengths for a specific sample preparation

#252091 Received 19 Oct 2015; revised 9 Jan 2016; accepted 2 Feb 2016; published 19 Feb 2016

protocol since scattering enhancement due to staining with absorbing dyes makes certain wavelengths more diagnostic than others [15].

$$\Sigma_{x,y} = \sqrt{\frac{1}{N_{x,y}} \sum_{i=1}^{N_{x,y}} (R(x,y)_i - \bar{R})^2} \tag{2}$$

2.5 Multi-wavelength analysis to generate an image of nanoscale disorder, (Σ_λ)

While the $\Sigma_{x,y}$ approach yields an equivalent term to the mean Σ of a region of interest, it does not generate an image of the nanoscale disorder in a sample in the manner that the traditional Σ analysis achieves. To allow for this spatial mapping of the nanoscale disorder a second new marker was developed (Σ_λ). This marker is calculated as the standard deviation of the reduced spectra at each pixel. Σ_λ is calculated using Eq. (3), where $R(\lambda)$ is the reflectance at the wavelength λ, and N_λ is the number of wavelengths in the spectrum (15). Σ_λ operates on the same principle as the full spectrum parameter, Σ, with the same central wavenumber, k_c, for Eq. (1). Information about the 3D nanoscale refractive index fluctuations is present in the spectrum of the scattered light and sampling wavelengths in 1nm increments in the visible spectrum oversamples this information. A sparse sampling and application of the same standard deviation calculation can achieve the same results only at the risk of a higher noise floor in the result.

$$\Sigma_\lambda = \sqrt{\frac{1}{N_\lambda} \sum_{i=1}^{N_\lambda} (R(\lambda)_i - \bar{R})^2} \tag{3}$$

For imaging purposes, a 2-D mean filter was applied to the resulting Σ_λ images within a 4x4 neighborhood to create an image that maps the nanoscale disorder within a sample. Mean filtering reduces noise and variability in the image due to the reduced length of the spectral data. Spatial image resolution is not decreased significantly by the mean filter since the pixel size at the sample plane (~182nm) is less than the diffraction limited resolution (~500nm).

2.6 Theoretical validation of the analysis

The newly proposed markers of nanoscale disorder were validated via numerical simulations of an experiment based on rigorous 3-D finite-difference time-domain (FDTD) solutions of Maxwell's equations [16]. To simulate wavelength-resolved microscope images of inhomogeneous samples, software implementation of the 3-D FDTD method called Angora was used [17, 18]. Bright-field, plane-wave epi-illumination microscope images with a light collection numerical aperture (NA) = 0.6 were synthesized for samples with a refractive index distribution resembling that of ethanol-fixed biological cells: average refractive index 1.53 [19, 20], spatial standard deviation of 0.05 [21], and a sample thickness 2μm. The spatial correlation of refractive index fluctuations was set to be exponential with correlation length (l_c) of 20 and 50nm, while the refractive indices of the top and bottom media were set to be 1 and 1.53 respectively. While this simulation models the case of an ethanol-fixed cell mounted on glass, the proposed markers are equally valid for any sample geometry where there is an opposing refractive index match and mismatch between the sample-medium interface and the sample-substrate interface, such as can occur in live-cell samples or tissue sections [7].

2.7 Experimental validation

Each of the proposed markers were also tested experimentally using data previously collected on the High-Throughput PWS system for full-spectrum analysis [13]. This included a case-control cell line experiment and two human-subjects cancer screening experiments. The cell line experiment used control vector (CV) HT29 human colorectal adenocarcinoma cells and epidermal growth factor (EGFR) knock-down HT29 cells as a less aggressive genetic variant.

#252091 Received 19 Oct 2015; revised 9 Jan 2016; accepted 2 Feb 2016; published 19 Feb 2016

The first human subjects experiment was a lung cancer screening experiment consisting of 23 patients, 9 with lung cancer and 14 age, sex, and smoking history matched controls. Buccal cells were collected by brushing from each patient's cheek and these brushings were then smeared onto a glass slide before being fixed in 95% ethanol and stained using Papanicolaou stain [13]. The second human subjects experiment included data from a prostate cancer risk assessment experiment. This consisted of 8 non-progressor patients (less aggressive cancer) and 10 progressor patients (aggressive cancer). Samples consisted of transrectal biopsies obtained with 3-D ultrasound guidance, fixed in ethanol, cut into four micrometer sections and mounted on glass slides [11]. All prostate tissue samples were confirmed to be histologically normal by a histopathologist.

2.8 Quantitative data analysis and statistical comparisons

For each data set, the raw data was processed by normalizing by the incident illumination, applying a low-pass Butterworth filter to remove noise, and subtracting a low-order polynomial fit from each normalized and filtered spectrum. The first diagnostic parameter, Σ, was calculated over the full-spectrum (500-700nm, 1nm sampling) at each pixel in the measured image. The mean Σ was then calculated over a region of interest (ROI) for each sample. Differences between the case and control groups were tested using Student's t-test and effect size was calculated as Cohen's d. For comparison, Σ_{λ} and $\Sigma_{x,y}$ were calculated using the same ROIs from each data set using the wavelengths corresponding to the sparse 15 wavelength spectrum, allowing results to be compared for all markers using the same data.

3. Results

3.1 System acquisition speed

System speed was improved by an order of magnitude through the implementation of sparse spectra acquisition and the corresponding analysis algorithms as summarized in Table 1. Collection of 251 wavelengths (500-700nm) took 21.44 seconds and analysis of those wavelengths took 14 seconds for a total time of 35.44 seconds per field-of-view. In contrast, the new reduced wavelength approaches required only 0.38 seconds to collect 15 wavelengths and 0.81 seconds for analysis for a total time of 1.19 seconds per field-of-view. This improvement of more than an order of magnitude in total analysis time makes possible a new approach for PWS screening. Instead of a four-step process consisting of slide-mapping, cell selection, image cube acquisition, and data analysis, the entire process can be completed in a single step through a whole-slide PWS (WSPWS) measurement. Thus, entire sample specimens and all cells on a slide can be visualized and quantitatively analyzed with PWS microscopy in the same time it took to previously acquire data for ~30 cells. With this method a 20mm^2 region on a slide can be measured and analyzed in less than 40 minutes.

Table 1. PWS system performance sparse spectrum vs. full-spectrum analysis

System	Acquisition Time per Cell (1 FOV)	Analysis Time per Cell (1 FOV)	Total Time per cell (1 FOV)
PWS (full-spectrum)	21.44s	14.00s	35.44s
WSPWS (sparse spectrum)	0.38s	0.81s	1.19s

3.2 Theoretical validation results

Numerically simulated wavelength-resolved microscope images generated using FDTD were analyzed according to the experimental analysis protocol. The ability of a well-established marker Σ to distinguish between samples with correlation lengths of 20 and 50nm was compared to that of the newly proposed markers. Figure 1(a) shows that all three parameters show effectively equivalent changes in magnitude over different correlation length scales

#252091 Received 19 Oct 2015; revised 9 Jan 2016; accepted 2 Feb 2016; published 19 Feb 2016

with slight variation in absolute value. All makers showed an increase of 65-66% from an l_c of 20nm to 50nm. In addition, the correlation of the magnitude of the new markers to Σ was evaluated over a range of different correlation lengths in Fig. 1(b). Both new markers, Σ_λ and $\Sigma_{x,y}$, showed strong correlation to Σ in response to changes in correlation length (*lc*) with R^2 >0.99. Small differences in absolute magnitude were also observable as offsets from the perfect one-to-one correlation.

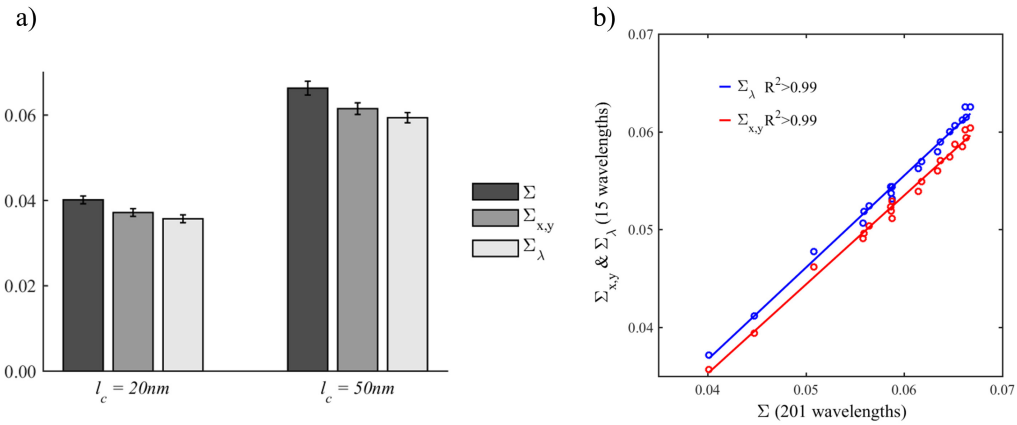

Fig. 1. (a) Comparison of the nanoscale sensitivities of newly developed markers Σ_λ and $\Sigma_{x,y}$ to that of Σ when measured from numerically simulated microscope images. All parameters show a 65-66% increase when the sample refractive index correlation length increased from l_c = 20nm to *lc* = 50nm. Uncertainty intervals correspond to the standard error between 20 samples created for each statistical condition. (b) Plot of the correlations of Σ_λ, and $\Sigma_{x,y}$, with the full-spectrum marker Σ. Σ_λ, and $\Sigma_{x,y}$ are determined using 15 wavelengths in the 500-700nm range, while Σ uses 1nm sampling in the same 500-700nm range. The values for the three parameters originate from simulations over a range of different refractive index correlation lengths between 20 and 50nm.

3.3 Experimental validation

For the HT29 cell line experiment, the mean values of each diagnostic parameter were calculated and compared. Figure 2 shows the mean Σ, $\Sigma_{x,y}$, and Σ_λ for the control group (smokers) and the lung cancer patients. The Σ was significantly higher for the lung cancer patients (p = 0.0026) with an effect size of 0.96. Similarly, Σ_λ was significantly higher for the lung cancer patients (p = 0.00024) with an effect size of 1.23. For $\Sigma_{x,y}$ the p-value was 0.00076 with an effect size of 1.12. Differences in the absolute values of mean Σ, $\Sigma_{x,y}$, and Σ_λ were observed within each of the experimental groups, which can likely be attributed to experimental variances including variations in focal plane selection, or temporal effects such as vibration in the sequentially acquired spectral data.

#252091 Received 19 Oct 2015; revised 9 Jan 2016; accepted 2 Feb 2016; published 19 Feb 2016

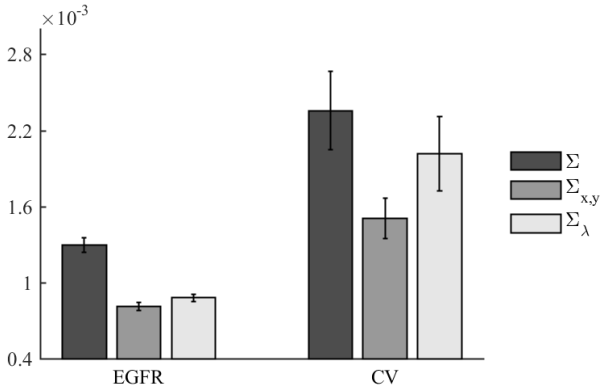

Fig. 2. The mean diagnostic parameter values for the full-spectrum analysis (Σ) and the reduced wavelength analyses ($\Sigma_{x,y}$ and Σ_{λ}) for the HT29 cell line experiment. All parameters were significantly higher for the CV cells compared to the EGFR cells. For the Σ the p-value was 0.0026 and the effect size was 0.96. For $\Sigma_{x,y}$, the p-value was 0.00076 with an effect size of 1.12. For Σ_{λ}, the p-value was 0.00024 and the effect size was 1.23.

For the lung cancer screening study, the mean diagnostic parameters were compared for the full-spectrum and the reduced wavelength methods. Figure 3 shows the mean diagnostic parameter values for both the full-spectrum analysis (Σ) as well as the reduced wavelength analysis $\Sigma_{x,y}$ and Σ_{λ} for the lung cancer experiment. The Σ was significantly higher for lung cancer patients than for the smoking controls (p = 0.037) with an effect size of 0.89. The Σ_{λ}, was also significantly higher for the lung cancer patients than for the smoking controls (p = 0.014) with an effect size of 1.02. The $\Sigma_{x,y}$ was also significantly higher (p = 0.015) with an effect size of 1.00.

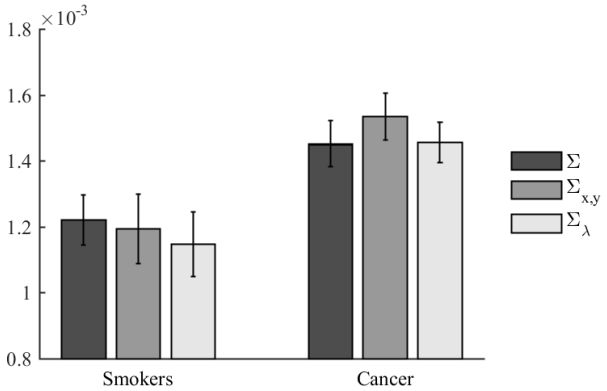

Fig. 3. The mean diagnostic parameter values for the full-spectrum analysis (Σ) and the reduced wavelength analyses ($\Sigma_{x,y}$ and Σ_{λ}) for the lung cancer diagnostics study. All parameters were significantly higher for the lung cancer patients compared to the smoker patients. For the Σ, the p-value was 0.037 and the effect size was 0.89. For $\Sigma_{x,y}$, the p-value was 0.015 and the effect size was 1.00. For Σ_{λ}, the p-value was 0.014 and the effect size was 1.02.

Accurate assessment of the risk of progression in prostate cancer is critical for proper treatment of the disease and reducing the number of unnecessary surgeries performed on patients. Σ has been shown to be sensitive to stages of the prostate cancer progression, making PWS a unique tool for this application [11]. Figure 4 shows the mean diagnostic parameters for patients that progressed to an aggressive form of prostate cancer and the non-progressor patients that remained with a less aggressive form of the disease that could be managed without surgery. The Σ was higher for the progressor patients, (p = 0.082) with an effect size

#252091 Received 19 Oct 2015; revised 9 Jan 2016; accepted 2 Feb 2016; published 19 Feb 2016

of 1.19. The Σ_λ was higher for progressor patients than nonprogressors, (p = 0.060) with an effect size of 0.92. The $\Sigma_{x,y}$ also was higher for progressors than nonprogressors with a p-value of 0.085 and an effect size of 0.086. In a recent larger study using a slightly different full-spectrum analysis technique, PWS differentiated between progressors and nonprogressors with p = 0.002, sensitivity = 88% and specificity = 72% [11].

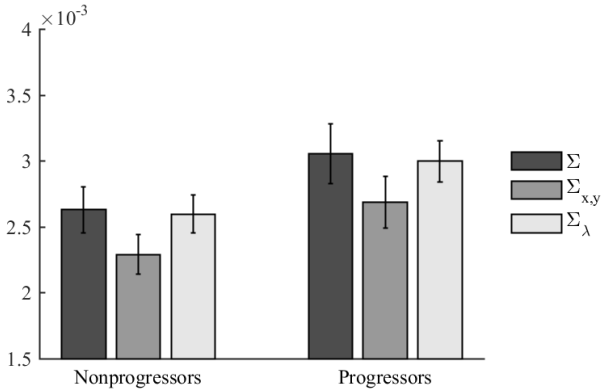

Fig. 4. The mean diagnostic parameter values for the full-spectrum analysis (Σ) and the reduced wavelength analyses ($\Sigma_{x,y}$, and Σ_λ) for the prostate cancer risk assessment experiment. All parameters were higher for the progressor patients than for the non-progressor patients. For the Σ, the p-value was 0.082 and the effect size was 0.84. For the $\Sigma_{x,y}$ parameter the p-value was 0.085 and the effect size was 0.86. For the Σ_λ parameter the p-value was 0.060 and the effect size was 0.92.

3.4 Proof-of-concept: whole-slide spectral nanocytology

To demonstrate the concept of whole-slide spectral nanocytology, a whole-slide nanoscale sensitive biomarker image was generated for one of the prostate tissue biopsy sections used in section 3.3 for the experimental validation. To generate this image only the 15 wavelengths used for the reduced wavelength analysis were collected allowing the whole slide spectral data to be collected in a comparable amount of time to a ~30 cell full-spectrum data set. Figure 5 shows Epi-illumination bright field and Σ_λ images for the same prostate tissue section. Red regions in the Σ_λ nanocytology image correspond to regions of high nanoscale disorder (refractive index fluctuations) and blue regions correspond to regions of low nanoscale disorder as shown by the scale bar in Fig. 5. This approach has several advantages over the previously used full-spectrum data acquisition and analysis approach. In terms of acquisition, nearly the entire cell population on a slide can be measured in the same time it previously took to measure only 30 cells. This is advantageous because analysis can be performed on the entire representative sample population, decreasing diagnostic variability and increasing the statistical power of the diagnosis. In addition, it is now possible to examine the distribution of nanoscale changes associated with cancer throughout an entire sample, particularly with large, multicellular samples such as tissue sections.

#252091 Received 19 Oct 2015; revised 9 Jan 2016; accepted 2 Feb 2016; published 19 Feb 2016

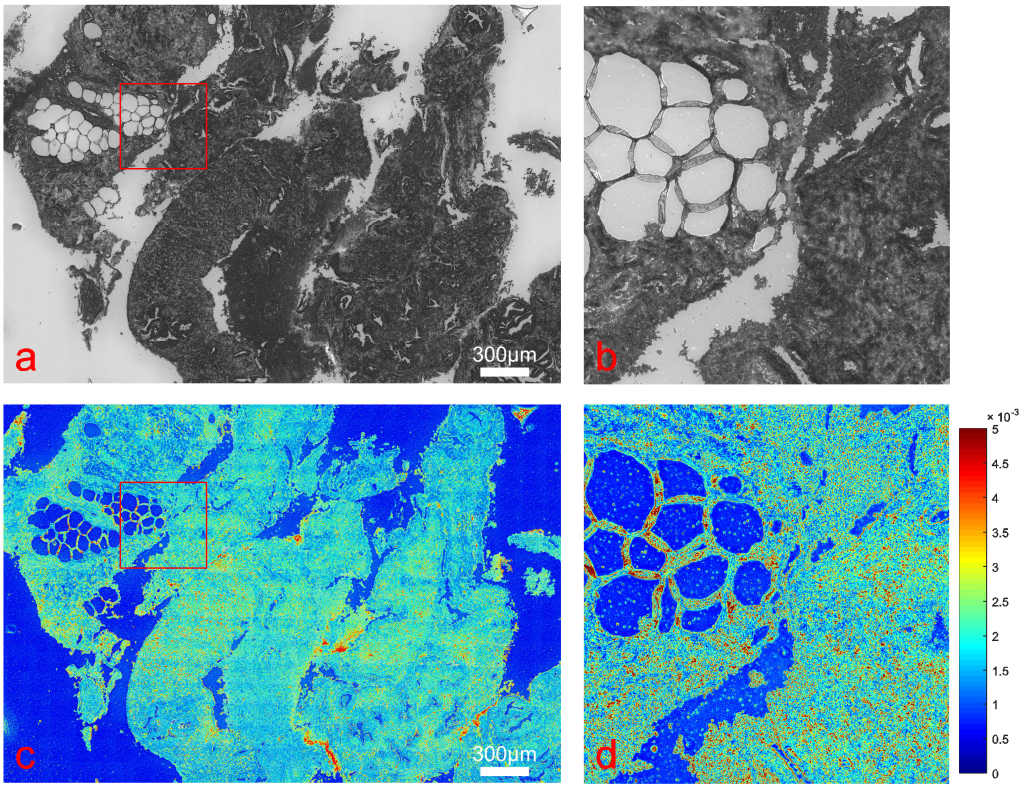

Fig. 5. Proof-of-concept Whole-Slide nanocytology image of a histologically normal prostate tissue biopsy section. (a) Grayscale Epi-illumination whole-slide bright field image of the tissue section. (b) Crop of red highlighted region in (a). (c) Σ_λ biomarker whole-slide image of the same prostate tissue section. Red regions correspond to regions of high nanoscale disorder (refractive index fluctuations) within the sample and the blue regions correspond to regions of low nanoscale disorder. (d) Crop of the red highlighted region in (c).

Other whole-slide microscopy techniques have been proposed for cancer screening applications via the field effect. Using DNA-specific staining, malignancy-associated changes have been detected and quantified as a biomarker for cancer screening using whole-slide microscopy [22]. This approach also was explored as a quantitative screening test for lung and breast cancer using the field effect [23]. The whole-slide PWS approach offers a label free alternative to these methods with nanoscale sensitivity to detect carcinogenesis in histologically normal-appearing samples. Because the PWS marker can be both label-free and quantitative it can be applied to multiple organ sites and tissue types without the need for the development of new staining protocols. In addition, it could be used in a multi-modal approach in conjunction with staining techniques in an attempt to improve the sensitivity and specificity of cancer screening for particular organs.

4. Conclusion

A reduction in the number of wavelengths required to sense refractive index fluctuations from the spectrum of a reflected light microscope has been demonstrated. Newly developed markers which use 15 wavelengths in the visible spectrum are sufficient to achieve sensitivity to nanoscale structures. Application of these markers to cancer screening experiments shows that changes in cells associated with carcinogenesis can be detected. The reduction in the number of wavelengths collected and analyzed yields an order of magnitude improvement in the time to acquire each frame in a spectral data cube (x,y,λ), enabling an approach for whole-

#252091 Received 19 Oct 2015; revised 9 Jan 2016; accepted 2 Feb 2016; published 19 Feb 2016

slide nanocytology. Whole-slide measurement can increase the statistical power of a diagnosis and will allow mapping of the nanoscale disorder in large samples such as tissue sections.

Acknowledgments

The authors would like to thank Justin Derbas and Charles Maneval for assistance with cell imaging. The results presented here are based upon work supported by the National Science Foundation Graduate Research Fellowship under Grant DGE-0824162, the National Institutes of Health under Grants: R01CA200064, R01CA155284, R01CA165309, and R01EB016983, the Nation Science Foundation Small Business Innovation Research program under Grant IIP-1214989, and the National Institutes of Health Small Business Innovation Research program under Grant 1R44CA168185. Drs. Subramanian and Backman are cofounders and/or shareholders in Nanocytomics LLC. All aspects of this study were done under the supervision of the Conflict of Interest Committee at Northwestern University.